ACS OMEGA

http://pubs.acs.org/journal/acsodf
Article

Biochar for Lead Ion Removal from Aqueous Solutions: the Effect of Inorganic Carbonate

Juan Tarlera, Ruiqi Li, Jonathan Lacuesta, Haiqiu Jiang, Tara Keyser, Deborah Page-Dumroese, Thomas Elder, Qiangu Yan, Zhiyong Cai, Mathew Smidt, and Yucheng Peng*

Cite This: https://doi.org/10.1021/acsomega.6c01646
Read Online
ACCESS | Metrics & More | Article Recommendations | Supporting Information

ABSTRACT: Biochar, a carbon-rich material that can be produced from forest byproducts and waste, is emerging as a valuable material for removing heavy metal ions from aqueous solutions. Biochar can be produced by many processes and equipment. Among these, mobile air curtain burners, developed to achieve lower levels of particulate matter and smoke than open pile burning, can be deployed in the field where biomass feedstocks are located. To elucidate lead metal ion (Pb^{2+}) removal mechanisms, this study characterized seven biochars generated by a novel mobile curtain burner, representing the first such investigation of materials produced by this platform. The Pb^{2+} removal capacities ranged from 35 to 224 $mg \cdot g^{-1}$ of biochar. To understand the factors influencing this removal capacity, various physicochemical properties of the biochars were characterized, including the specific surface area, electrical conductivity, zeta potential, and pH. The mineral content, particularly calcium carbonate ($CaCO_3$), was determined by analyzing the X-ray diffraction (XRD) patterns of the biochar samples using the Rietveld refinement method. Quantitative analysis showed that $CaCO_3$ was the primary driver in Pb^{2+} removal. Precipitates of cerussite and hydrocerussite crystals were observed in the biochar XRD patterns after Pb^{2+} removal. A linear correlation was observed between the Pb^{2+} removal capacities of these biochars and the $CaCO_3$ contents. The results indicate that the Pb^{2+} removal capacities of these biochar samples were predominantly determined by the $CaCO_3$ contents through the chemical precipitation mechanism.

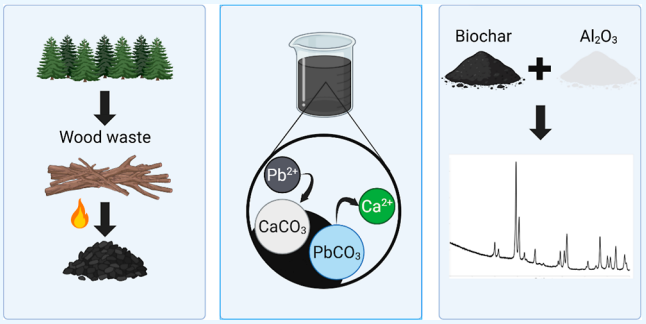

1. INTRODUCTION

Heavy metal pollution is a growing concern due to increasing levels of these pollutants in the environment.[1] The presence of these metals, especially in their ionic forms, can be detrimental to human health and agricultural activities.[2−4] Heavy metals tend to bioaccumulate in flora and fauna, causing irreversible damage to metabolic and neurological functions.[5] Among the heavy metals of concern, lead is one of the most commonly found contaminants in water and soil, entering water and soil mainly through anthropogenic activities such as mining, smelting and battery manufacturing.[6,7]

The removal of heavy metals from contaminated water can be achieved through various technologies such as membrane filtration, ion exchange resins and electrochemical deposition.[8,9] Some more modern techniques have also been developed, using biocatalytic and enzymatic mechanisms to remove Pb^{2+} from wastewater.[10,11] When comparing all of these technologies, the use of sorbents is arguably the most cost-effective option.[8,9] With its high efficiency, low cost, reusability, and, in the case of organic-based sorbents, sustainable production, sorbent-based technology has been one of the most investigated alternatives for heavy metal water remediation.[8,9,12−15] The performance is usually dependent on pH, adsorbent dose, contact time, temperature, particle size, and stirring or mixing speed.[16] Biochar is one of these sorbents, and it has been extensively studied as a heavy metal remediation agent. It is a sustainable material which can be cheaply produced from various feedstocks including many types of organic waste.[17] Biochar has already been effectively applied to heavy metal remediation in water systems, among other applications.[18−25] Due to the high cost of transporting low-value forest residues, large-scale biochar production may be financially unfeasible.[26] As a result, portable conversion platforms have been proposed to produce biomass-based products closer to the supply. Among these, air curtain burners offer an effective solution for processing biomass residues and producing biochar. This process results in more complete and cleaner combustion compared to traditional methods, such as open pile burning.[27] A significant advantage over open pile

Received: February 11, 2026
Revised: July 13, 2026
Accepted: July 17, 2026

burning is the ability to operate under various weather conditions, which extends the burning season for residue disposal. This method not only helps in the disposal of forest residues that contribute to reduce wildfire risk but also creates an economical and environmentally beneficial product.[28,29]

Despite its widespread application, underlying sequestration mechanisms remain a subject of debate.[30−32] While it is generally accepted that removal occurs through a combination of surface adsorption, ion exchange, electrostatic attraction and chemical precipitation, the relative contribution of each pathway is often complex to define.[30,31] Studies have highlighted the importance of chemical precipitation as a primary mechanism for removing various heavy metals, particularly lead, which is primarily influenced by the mineral content of the biochars, such as carbonates and phosphates.[33−35] However, a significant gap exists in the literature. Few studies have quantified the mineral content of biochar, and among those, even fewer have established a quantitative relationship between the mineral content and the heavy metal removal capacity.[35−38] Simultaneously, detailed characterization of the mineral fraction is essential for identifying the dominant removal mechanism. Quantifying reactive phases like carbonates can help determine relative contributions of chemical precipitation when compared with other mechanisms.[39]

This study addresses this gap by employing Rietveld refinement on X-ray diffraction (XRD) patterns to quantify the mineral content. XRD is a replicable, nondestructive method for both qualitative and quantitative analysis of crystalline and amorphous samples that can be applied to characterize biochar.[40] This methodology can be coupled with Rietveld refinement, a full pattern fitting method which can be used to quantify crystalline phases of materials in mixtures.[41,42] For highly amorphous samples, quantitative Rietveld refinement requires the addition of an internal standard, a highly crystalline, chemically inery compound to be added in a known proportion. This standard must have well-defined diffraction peaks that do not overlap with the sample's compound peaks.[43,44] The most used compounds are α-aluminum oxide (Al_2O_3), zinc oxide (ZnO) or rutile (TiO_2).[44,45] By integrating internal standards to account for the amorphous carbon matrix, this approach allows for the establishment of a quantitative relationship between the biochar's mineral content and lead metal ion (Pb^{2+}) removal capacity.

The goal of this study was to establish a correlation between the properties of 7 biochars produced by the air-curtain burner system and their Pb^{2+} removal capacity. The biochars, produced from various wood and lignocellulosic residues, were characterized for several key properties. Their Pb^{2+} removal capacities, as well as their calcium carbonate ($CaCO_3$) content, pH, electrical conductivity (EC), Zeta potential (ZP), specific surface area (SSA), and elemental compositions were determined. The $CaCO_3$ content in the biochar samples was quantified by Rietveld refinement of XRD patterns, a method previously unreported for biochar analysis. Additionally, XRD and Scanning Electron Microscopy (SEM) coupled with Energy Dispersive X-ray Spectroscopy (EDS) studies confirmed the formation of lead-based carbonates after biochar uptake in aqueous solutions. The results demonstrated that a linear relationship exists between $CaCO_3$ content and biochar's Pb^{2+} removal capacity. While multiple mechanisms are likely to contribute to the Pb^{2+} removal process, the strength of this relationship coupled with the identification of lead carbonate minerals points toward chemical precipitation as a primary driver of removal for these biochars. These findings highlight the importance of quantifying the mineral fraction when evaluating removal agents' performance, helping the community better understand the predominant mechanisms of heavy metal ion removal in aqueous solutions using biochar and offering insights into the design and application of biochar-based remediation strategies.

2. MATERIALS AND METHODS

2.1. Materials

The seven biochar samples were produced by a CharBoss unit, a portable air curtain burner developed under a Cooperative Research and Development Agreement (CRADA) between Air Burners (Palm City, FL) and the US Forest Service. The biochars that were used in this work and the information available on the feedstocks from which they were produced are listed in Table 1. Samples I, II, and VII were produced during demonstrations of the CharBoss system, using feedstocks available on-site, while samples III−VI were produced using known proportions of specific wood species. Due to the operational nature of these field demonstrations, measurements of production temperatures, residence times and oxygen availability were not performed. The CharBoss system was designed as a field-deployable solution for disposing of forestry byproducts rather than an analytical-grade furnace where atmospheric conditions are strictly monitored. Consequently, this study focuses on characterizing the resulting materials to define their properties, rather than evaluating the specifics of the production process. There was also a limited control over the materials used for biochar production (see Table 1). In all cases, the feedstock used to produce the biochar was representative of typical wood waste management operations. Because of this, it is likely that the samples included bark and other types of impurities, such as sand from dragging logs through the ground. Lead chloride ($PbCl_2$) with a 99% purity and Al_2O_3 with a 99.997% purity were purchased from Thermo Fisher Scientific, and deionized water was used to prepare all suspensions and dilutions.

Table 1. Biochar Samples Information

biochar sample	feedstock type	collection and production location
I	hardwood	ouachita national forest, OK/AR
II	municipal mixed tree trimmings and green waste	tooele county landfill, tooele, UT
III	maple	bent creek experimental forest, NC
IV	60% white oak, 40% red oak	bent creek experimental forest, NC
V	40% oak, 20% yellow poplar, 10% red maple, 10% other	bent creek experimental forest, NC
VI	yellow poplar	bent creek experimental forest, NC
VII	cedar, douglas-fir	vida, OR

2.2. Biochar Characterization

2.2.1. Sample Preparation. To ensure a consistent particle size, biochar samples were ground to a powder using the PTA-2 Ball Mill (Shimpo-Nidec Corporation, Kyoto, Japan) and a mortar and pestle. Then, the biochar powders were passed through a 140-mesh (105 μm) sieve (Sargent-Welch Scientific Company, Skokie, IL, USA). This particle size was used in all experiments unless otherwise specified.

2.2.2. pH and Electrical Conductivity. The biochar powder was suspended in deionized water at a solid to liquid weight ratio of 1:10. The suspensions were shaken in an MX-RL-E tube rotator (Scilogex, Rocky Hill, USA) at 40 rpm for 1 h, and then the suspension was left to settle for 1 h before measurement. An Extech EC600 pH/

https://doi.org/10.1021/acsomega.6c01646
ACS Omega XXXX, XXX, XXX−XXX

conductivity sensor (Teledyne FLIR LLC, Wilsonville, OR, USA) was used to measure both pH and EC. Three replicate readings were performed for each sample, and the average was calculated.

2.2.3. Specific Surface Area. The biochar samples were prepared by degassing under vacuum at 200 °C for 24 h to remove adsorbed moisture and gases without inducing thermal degradation or structural changes using a VacPrep 061 instrument (Micrometrics, Norcross, GA, USA). The N_2 gas adsorption isotherms were then measured at −196 °C using a Micromeritics TriStar II Plus (Norcross, GA, USA). Measurements were taken across a relative pressure range between 0.005 and 0.5, with three replicates performed for consistency. The surface area was calculated using the Brunauer−Emmett−Teller (BET) method according to the following equation

$$\frac{1}{W\left(\left(\frac{P}{P_0}\right)-1\right)} = \frac{1}{W_m C} + \frac{C-1}{W_m C}\left(\frac{P}{P_0}\right) \quad (1)$$

Where W is the cumulative volume of gas adsorbed at standard temperature and pressure, P and P_0 represent the equilibrium pressure and the saturation vapor pressure of the adsorbate at the temperature of adsorption, respectively, W_m is the volume of gas required to form a complete, theoretical monomolecular layer over the entire surface of the biochar and the dimensionless C constant, indicates the energy of adsorption.

2.2.4. Zeta Potential. Biochar samples were ground using a PTA-2 Ball Mill (Shimpo-Nidec Corporation, Kyoto, Japan) and a mortar and pestle. The samples were passed through a 200-mesh (74 μm) N0.10 sieve (Sargent-Welch Scientific Company, Skokie, IL, USA) to obtain smaller particles, which are more stable in suspension for measuring zeta potential,[46] and then loaded into polyethylene tubes. Deionized water was added to suspend the biochar at a solid-to-liquid weight ratio of 1:500 to obtain a stable, nonturbid suspension. The suspensions were then shaken with an MX-RL-E tube rotator (Scilogex, Rocky Hill, USA) and rotated at 40 rpm for 1 h before loading them into DTS1070 cells (Malvern Panalytical, Malvern, UK) to measure the ZP using a Zetasizer Lab (Malvern Panalytical, Malvern, UK). ZP was measured at room temperature at the native pH of the suspension in DI water, and five consecutive readings were performed continuously for each sample, with the mean reported.

2.2.5. Elemental Analysis. The C, N, and H contents of the biochar samples were analyzed with a FLASH 2000 CHNO analyzer (Thermo Fischer Scientific, Waltham, MA, USA). Oxygen content was calculated by difference. It should be noted that this calculation yields an 'apparent' oxygen content, as it incorporates oxygen atoms from both the organic carbon matrix and the inorganic mineral phases. The oxygen to carbon (O/C) and hydrogen to Carbon (H/C) ratios are calculated and expressed as molar ratios.

2.2.6. Pb^{2+} Removal Capacity. A kinetic study was performed to determine the Pb^{2+} removal behaviors by biochar. In the kinetic study, 100 mg of biochar sample was placed in a 50 mL polypropylene tube to which 50 mL of a 700 mg·L^{-1} solution of $PbCl_2$ was added. The initial and residual Pb^{2+} concentrations in the aqueous solutions were measured using a ultraviolet visible light (UV−vis) spectrophotometer (UV-1600PC, Avantor Inc., Radnor, Pennsylvania, USA) at a wavelength of 208 nm following a procedure used by Peng et al.[47] This method was validated in the range of 1−30 mg·L^{-1} establishing a calibration curve correlating the intensity of the UV wavelength with the Pb^{2+} concentrations. The tubes were placed in an MX-RL-E tube rotator (Scilogex, Rocky Hill, USA) and rotated at 40 rpm for 72 h at room temperature. Samples of the suspension were taken at 10, 30, 60, 120, 180, 240, 480, 1140, 2880, and 4320 min and filtered through 0.22 μm hydrophilic PTFE filters. The residual Pb^{2+} concentration in the filtered solution was determined using the same UV−vis spectrophotometric procedure used for the initial concentration. Based on the amount of lead ions (Pb^{2+}) in the filtrate, a pseudo-second-order model was used to fit the data, with the equilibrium removal capacity (q_e) representing the removal capacity of the biochar. This model was selected based on literature where the rate-limiting step is a chemical interaction rather than a physical diffusion process.[48,49]

2.2.7. XRD Analysis of Biochar. For the analysis of pristine biochar samples, were analyzed with a SmartLab X-ray diffractometer (Rigaku Corporation, Tokyo, Japan), with Ni-foil filtered Cu K-alpha radiation, which has a wavelength of 0.154 nm. The X-ray tube operates at 40 kV and 30 mA, using a compact photon-counting X-ray detector (HyPix-3000). The samples were scanned over a 2-theta range of 10 to 80 degrees at a scan speed of 10°·min^{-1}. One sample, for which limited material was available, was scanned at a rate of 5°·min^{-1}. This difference in scan speed was not found to significantly affect the qualitative phase analysis, as for all scans the main diffraction peaks were well resolved and defined.

For the analysis of lead mineral formation on biochar, 100 mg of sample from all biochars were placed in 50 mL polypropylene tubes to which 50 mL of a 700 mg·L^{-1} $PbCl_2$ solution was added. Similar to the Pb^{2+} removal capacity studies, the suspensions were shaken in the same tube rotator at 40 rpm for 72 h at room temperature. The biochar was then separated by centrifugation, with the suspension transferred into 15 mL glass tubes and spun at 4000 rpm for 10 min in a LC-8 Lab Centrifuge (Benchmark Scientific Inc., Sayreville, NJ, USA). The biochar in the glass tubes was dried at 105 °C in a convection oven (Cole-Parmer, Vernon Hills, IL, USA) for 24 h. The biochar powder samples were analyzed in triplicate with the SmartLab X-ray diffractometer (Rigaku Corporation, Tokyo, Japan) with the same operational parameters as before, and a scanning speed of 10°·min^{-1}.

The $CaCO_3$ content for the different biochar samples was determined by mixing 100 mg of each biochar with 10 mg of Al_2O_3. The mixture was thoroughly homogenized by vigorous hand shaking. The samples were scanned over the same 2-theta range of 10 to 80 degrees at a scan speed of 2.5°·min^{-1}. This lower scanning speed was chosen to obtain higher-quality data for quantification purposes, as supported by the literature.[42] For each biochar sample, three replicates of the homogenized mixture were prepared and analyzed.

Rietveld refinement of the X-ray diffraction data was performed using the open-source software Profex (version 5.5.0), which serves as a graphical user interface for the fundamental parameters-based Rietveld program BGMN.[50] The phases for the Rietveld refinement were selected based on previous qualitative analysis of the patterns, which were used to identify the constituents. In addition, two amorphous peaks were included in the refinement at the 2θ angles of 25° and 43° to represent the two characteristic broad amorphous carbon peaks in the ranges of 20−30° and 40−50°.[51] The internal standard weight ratio (Al_2O_3) was specified before starting the refinement. After fitting each phase, a calculated pattern for the whole sample was generated by summing the individual patterns for all the identified phases, with the respective weight ratios calculated from the internal standard weight ratio. The quality of the refinement was judged mainly through the χ^2 value, where values close to 1 indicate a good fit.[52,53] In addition, a visual analysis was performed between the experimental and calculated patterns to confirm that any differences were confined to the identified peaks and not caused by unmodeled phases.

2.3. SEM-EDS

Surface morphology and elemental composition were characterized via SEM-EDS using a ZEISS EVO 10 scanning electron microscope (Carl Zeiss AG, Germany) equipped with an EDAX TEAM Element EDS system (USA). Biochar sample I, both pristine and after Pb^{2+} exposure, were mounted onto aluminum stubs using double-sided conductive carbon adhesive tape. Images using Secondary Electrons (SE) and Backscattered Electrons (BSE) were obtained, as well as EDS point composition information for certain structures. Images were acquired at an accelerating voltage of 20 kV and a working distance of approximately 11 mm. Morphological details were resolved using a Secondary Electron (SE1) detector, while elemental contrast was highlighted using a High Definition Backscattered Electron (HDBSD) detector.

https://doi.org/10.1021/acsomega.6c01646
ACS Omega XXXX, XXX, XXX−XXX

2.4. Statistical Analysis

All statistical analyses were performed using R (v4.4.1) to evaluate the collected data. For each measured property, a one-way analysis of variance (ANOVA) was conducted to test for significant differences in mean values across the seven biochar samples. In cases where the ANOVA indicated a significant effect ($p < 0.05$), a Tukey's HSD posthoc test was performed to identify which specific pairs of biochar samples were statistically different from one another. The relationship between the measured biochar properties and Pb^{2+} removal capacity (q_e) was investigated using correlation and regression analyses. A simple linear regression model was used to analyze such relationships, and the coefficient of determination (R^2) was calculated in each case.

3. RESULTS AND DISCUSSION

3.1. Biochar Properties

The properties of all seven samples were measured to assess their physicochemical characteristics. Line plots with the mean values and standard deviations are shown in Figures 1, 2, and 3.

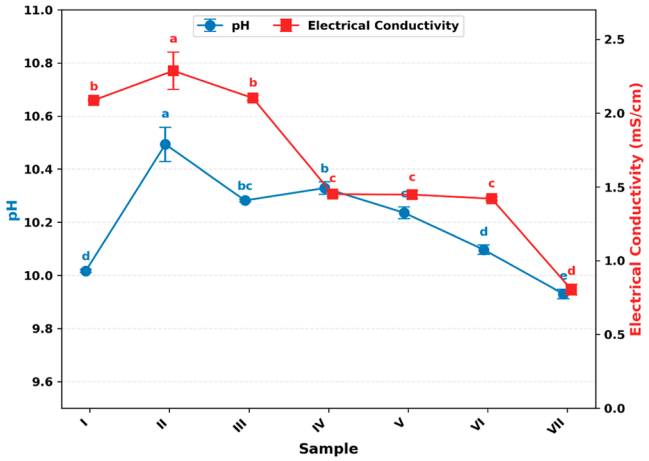

Figure 1. pH and EC for different air curtain burner biochar samples.

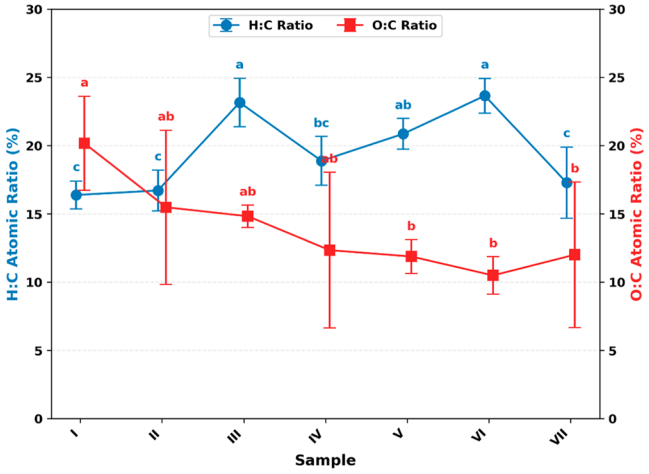

Figure 2. H/C and O/C ratios for different air curtain biochar samples.

One-way ANOVA confirmed that all biochar samples were statistically different from at least one other sample for every property analyzed. Tukey's HSD posthoc test results are included in the line plots, with different letters indicating statistically significant differences ($p < 0.05$).

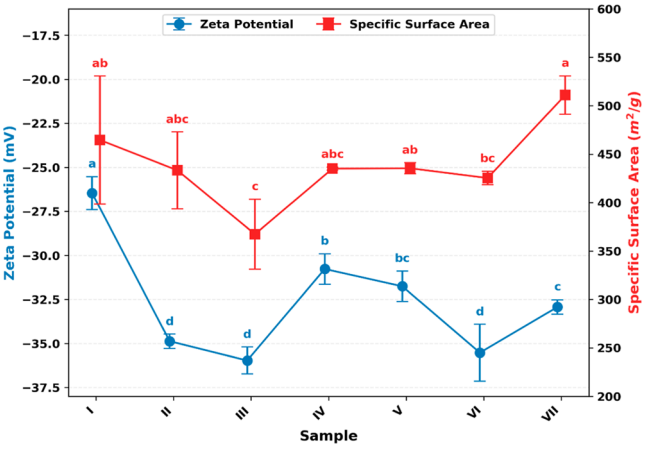

Figure 3. ZP and SSA for different air curtain biochar samples.

The pH values show that all biochars have an alkaline nature, which is consistent with the literature. Chen et al. measured biochar pH produced using fir sawdust and found pH values ranging from 6.74 to 9.59, depending on pyrolysis temperature.[54] Yargicoglu et al. measured pH for biochars produced from pine, a mixture of fir and pine, and a mixture of aged hickory and oak, finding values of 8.47, 8.77, and 7.88, respectively.[55] Jiang et al. found the pH of jarrah hardwood biochar to be considerably greater than softwood pine biochar, with values of 9.9 and 7.8, respectively, which would follow the same trend as our data.[56] The pH values for all the samples in this study are greater than 9.93, with the greatest pH value of 10.49. The high pH values of the biochar samples can be primarily attributed to the presence of $CaCO_3$ in all these samples (as demonstrated by the XRD analysis in Section 3.3.3) with $CaCO_3$ having a well-documented alkaline nature.[57] However, even with XRD analysis only identifying the presence of $CaCO_3$, the pH values could also reflect the presence of other alkaline elements such as K, Mg and Na not detected by XRD. Biochar pH is inherently correlated with the formation of carbonates and the content of inorganic alkalis derived from the feedstock and pyrolysis conditions.[57] This high pH generated by the biochar samples can become a significant driver for Pb^{2+} removal. The high pH shifts inorganic carbon speciation to favor CO_3^{2-} ions, facilitating the chemical precipitation of lead as insoluble mineral phases. EC values spanned a considerable range, from 2.29 to 0.80 dS·m^{-1}. Jiang et al. measured EC for biochars produced from pine and jarrah wood, also finding a wide range of values from 2.22 to 0.32 dS·m^{-1}, attributing this difference to the accumulation of soluble salts in the feedstock, depending on the growth environment and conditions.[56] The EC in solution produced by biochar is proportional to the concentration of dissolved mineral salts in the aqueous phase.[58] In these biochar systems, EC can measure the release of alkaline species and ions, which can influence chemical precipitation of Pb^{2+}. ZP showed negative values for all biochars, with most reaching values below −30 mV. Biochar typically exhibits a negative surface charge due to oxygen-containing functional groups, such as carboxyl groups, which results in negative ZP values.[59,60] Yargicoglu et al. also determined the ZP of biochars produced by a pyrolysis process from pine, a mixture of fir and pine, and a mixture of aged hickory and oak, obtaining values of −23.7, −15.8, and −15.4 mV, respectively.[55] ZP is closely related to solution pH, so comparisons without pH control should be

https://doi.org/10.1021/acsomega.6c01646
ACS Omega XXXX, XXX, XXX−XXX

interpreted with caution.[60] However, the zeta potential is still a good indicator of the surface charge which affects possible electrostatic interactions.[61] All samples showed a negative zeta potential, possibly facilitating the initial attraction of Pb^{2+} cations to the biochar surface. SSA values were high when compared with other nonactivated biochars. Jiang et al. determined SSA for pine and jarrah wood biochar, obtaining values of 219 and 309 $m^2 \cdot g^{-1}$, respectively.[56] Yargicoglu et al. found that for pine wood biochar, the SSA were even lower, reaching up to only 41 $m^2 \cdot g^{-1}$[55]. According to a review by Tomczyk et al. softwood biochars show higher SSA than hardwood biochars, consistent with our results with biochar VII, the only sample produced from softwood species, showing the highest SSA values out of the seven samples.[57] It has been well documented that SSA is highly dependent on the biochar manufacturing process and conditions, with higher temperatures increasing SSA, which could explain these differences.[57] Biochar surface area is typically associated with physical adsorption capacity, and several authors claim it to be one of the main predictors in heavy metal removal, arguing that higher surface areas allow for improved interactions between metal ions.[30] While H/C and O/C ratios are usually inversely proportional to pyrolysis temperature as water and volatiles are released, the raw material's inherent composition plays an equally crucial role in determining these values.[62] Jiang et al. found H/C and O/C ratios for hardwood and softwood biochars, with softwood having an H/C of 46% and an O/C of 14%, while hardwood presented an H/C of 23% and an O/C of 8%.[56] Keiluweit et al. measured H/C and O/C ratios of biochar manufactured from Ponderosa pine shavings between temperatures of 100 °C (drying) and 700 °C, obtaining values of 159% and 21% for H/C, and 63% and 5% for O/C.[62] The H/C ratios obtained for most of the biochars used in this study are below this range, while O/C values are within the low end of the range.

3.2. Removal Kinetics

The Pb^{2+} removal kinetic data from aqueous solutions by biochar were successfully fitted with a pseudo-second-order model, consistent with other Pb^{2+} removal studies.[63−65] While this model is often associated with chemisorption-controlled processes, it is utilized here as an empirical framework to determine the equilibrium removal capacity and facilitate quantitative comparisons between the different biochar samples. This empirical approach focuses on the overall rate of Pb^{2+} removal from the solution without assuming a specific surface-adsorption mechanism. The linearized form of the model is shown in eq 2.

$$t/q_t = 1/k_2 q_e^2 + t/q_e \quad (2)$$

Where $q_t$corresponds to the amount of Pb^{2+} removed per unit mass of biochar at a time t, q_e is the amount of Pb^{2+} removed at equilibrium and $k_2$is the pseudo-second order rate constant.

In general, the kinetic process exhibited rapid initial removal rates, reaching approximately 80% of the maximum Pb^{2+} removal capacity within 4 h in virtually all cases. Between 48 and 72 h, practically no difference was detected in the residual Pb^{2+}concentration in the solutions. At this point, the system was considered to have reached equilibrium. Figure 4 displays the kinetic curves for the Pb^{2+} removal by different biochar samples. The removal capacities for all biochars, as shown in Figure 5, vary significantly between samples. The maximum Pb^{2+} removal capacity of 224 ± 3 $mg \cdot g^{-1}$ biochar corresponds

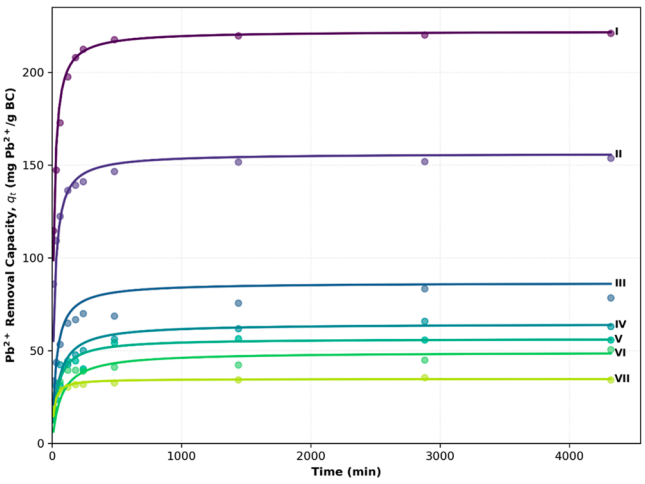

Figure 4. Kinetic curves for different air curtain burner biochar samples.

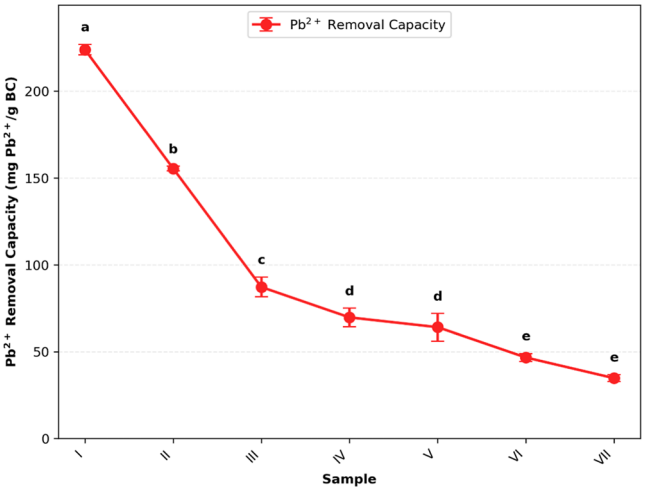

Figure 5. Pb^{2+} removal capacity for different air curtain burner biochar samples.

to sample I, while sample VII has the minimum removal capacity, with 35 ± 3 $mg \cdot g^{-1}$ biochar. These values are generally above what has been previously reported when using unmodified wood-based biochar for Pb^{2+}removal. Table 2 provides a summary of reported Pb^{2+} removal capacities for wood-based modified and unmodified biochars including feedstock used and production conditions.

The data presented in Table 2 demonstrates that the CharBoss biochars exhibit Pb^{2+} removal capacities that meet or exceed those of several previously reported biomass-derived chars. Notably, the performance of the high-performing CharBoss samples is competitive even with biochars that have undergone postproduction chemical or physical modifications designed to enhance their performance. However, because removal capacities depend on specific experimental parameters, such as initial Pb^{2+} concentration, solution pH, and solid-to-liquid ratio, these values are not directly comparable across disparate studies. Nevertheless, the high capacity observed for the unmodified air-curtain burner biochars under the current conditions suggests a robust potential for lead remediation driven by their intrinsic mineral content.

https://doi.org/10.1021/acsomega.6c01646
ACS Omega XXXX, XXX, XXX−XXX

Table 2. Comparison of Pb^{2+} Removal Capacities and Identified Removal Mechanisms for Wood-Based Biochars

feedstock	modification	concentration range ($mg·L^{-1}$)	temperature (°C)	residence time (h)	removal capacity ($mg·g^{-1}$)	mechanism	reference
hickory chips	-	2−250	600	2	11.2	-	64
hickory chips	NaOH	2−250	600	2	53.6	-	64
douglas fir green wood chips	KOH	25−1000	900,1000	1−10 s	140	complexation to surface groups	66
hickory chips	$KMnO_4$	100	600	1	153.1	surface adsorption mechanisms	67
commercial hickory chips	-	2−250	350,450,600	2,3,5	12.2−16.3	cation exchange	68
shredded wood	-	15−155	475	0.25	0.09−2.44	cation exchange	69
shredded wood	Mild air oxidation	15−155	475	0.25	1.04−9.28	cation exchange	69
aak wood	$Fe_2(SO_4)^{3+}$ $FeSO_4$	1−100	400,450	30 s	30.20−55.91	metal complexation	70
oak bark	$Fe_2(SO_4)^{3+}$ $FeSO_4$	1−100	400,450	30 s	8.92−10.13	metal complexation	70
oak wood	-	2−1000	400,450	30 s	2.62	cation exchange	71
pine wood	-	2−1000	400,450	30 s	4.13	cation exchange	71
oak bark	-	2−1000	400,450	30 s	13.1	cation exchange	71
pine bark	-	2−1000	400,450	30 s	3	cation exchange	71
loblolly pine	-	20	350,450,600	-	1.8−3	electrostatic interaction, precipitation and surface complexation	72
hamlin citrus	-	20	350,450,600	-	7.6−7.9	electrostatic interaction, precipitation and surface complexation	72
virgin coniferous wood	-	50,100	600	-	20.15	-	73
soft wood pellets	-	1000	550	-	8.0808	surface precipitation	74
british broadleaf hardwood	-	1000	600	13.5	47.656	surface precipitation	74

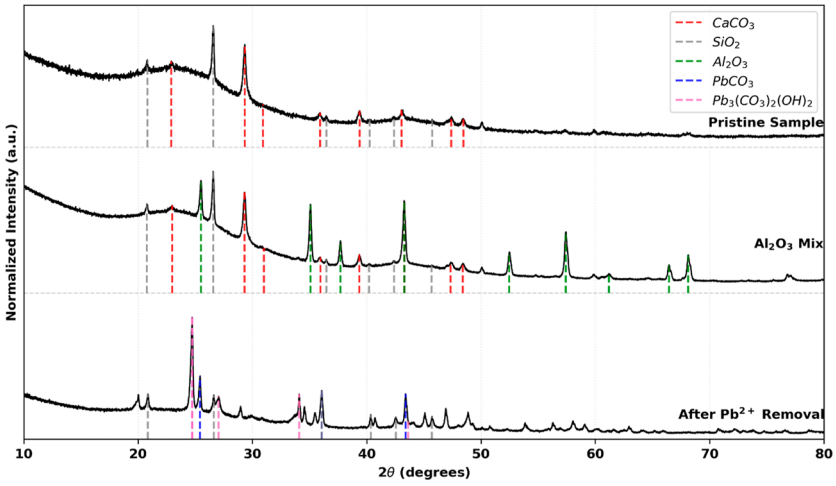

Figure 6. XRD patterns for biochar sample I with phase identification.

3.3. XRD Analysis of Biochar

3.3.1. Pristine Biochar Analysis. The XRD scans of the seven biochar samples appeared to be mostly amorphous, with two broad peaks at 2θ angles of approximately 25° and 43°. Additionally, the presence of calcium carbonate ($CaCO_3$) and quartz (SiO_2) was detected. The main peaks used for the identification of these materials were at 2θ angles of 29.4° and 39.4° for $CaCO_3$ and 26.6° for SiO_2.[51,75] Biochar sample III was scanned at a different scanning speed of $5°·min^{-1}$ due to the limited amount of sample. However, as can be seen here, no significant differences in data quality can be observed between this pattern and the others.

3.3.2. Lead Mineral Formation on Biochar. The XRD patterns of the seven biochar samples after Pb^{2+} removal showed two broad amorphous carbon peaks. In addition, all samples showed the presence of lead minerals, cerussite ($PbCO_3$) and/or hydrocerussite ($(Pb)_3(CO_3)_2(OH)_2$). Since the main peak for both $PbCO_3$ and $(Pb)_3(CO_3)_2(OH)_2$ has virtually the same location at a 2θ angle of 24.7°, a visual assessment of these phases' presence and prevalence is difficult when only considering this peak. Therefore, other smaller peaks were selected to visually identify the phases. The selected peaks for the phases can be seen at 2θ angles of 34.1° for $(PbCO_3)_2Pb(OH)_2$ and 25.4°, 36.0° and 43.4° for $PbCO_3$.[76] The presence of these two phases of lead compounds is consistent with the literature, indicating that they can coexist and are stable over a wide range of pH values.[77]

Pristine biochar samples with higher $CaCO_3$ peak intensities showed stronger peaks for lead carbonate minerals. This

https://doi.org/10.1021/acsomega.6c01646
ACS Omega XXXX, XXX, XXX−XXX

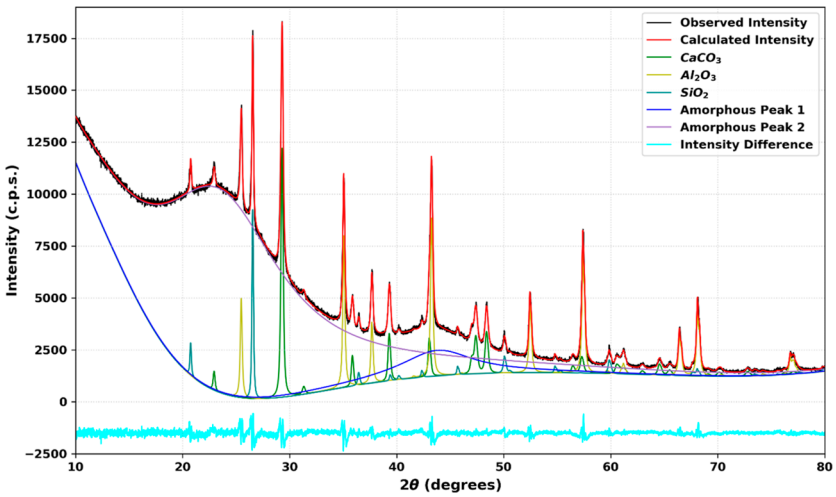

Figure 7. Rietveld refinement plot for biochar sample I.

mechanistic link indicates that $CaCO_3$ in the biochar serves as the primary reactant for the formation of lead carbonate minerals, which is consistent with the reaction pathways shown in eqs 3 to (5)[33]

$$CaCO_{3(s)} \leftrightarrow Ca^{2+}_{(aq)} + CO^{2-}_{3(aq)} \quad (3)$$

$$2CO^{2-}_{3(aq)} + 3Pb^{2+}_{(aq)} + 2OH^{-}_{(aq)} \leftrightarrow Pb_3(CO_3)_2(OH)_{2(s)} \quad (4)$$

$$CO^{2-}_{3(aq)} + Pb^{2+}_{(aq)} \leftrightarrow PbCO_{3(s)} \quad (5)$$

These results suggest an important relationship between the $CaCO_3$ content and Pb^{2+} removal capacity. No monitoring of Ca^{2+} or carbonate/bicarbonate species release was performed, representing a limitation when it comes to the understanding of underlying removal mechanisms. However, the consumption of crystalline $CaCO_3$ alongside the emergence of $PbCO_3$ phases provides robust evidence that chemical precipitation could be a major mechanism in Pb^{2+} removal for these samples.

3.3.3. $CaCO_3$ Content. To determine the $CaCO_3$ content, the patterns were first quantitatively analyzed to identify the crystalline phases present in each sample. All seven biochar samples showed evidence of $CaCO_3$ and silicon dioxide (SiO_2) in the form of quartz. All samples showed clear evidence of the added internal standard, Al_2O_3, with peaks clearly visible at 2θ angles of 25.5°, 35.1°, 43.3°, and 57.4°. Figure 6 presents three XRD patterns for biochar sample I: pristine, mixed with an Al_2O_3 internal standard for quantification, and after Pb^{2+} exposure. XRD patterns of the pristine sample, mixed with an Al_2O_3 internal standard, and after Pb^{2+} exposure for all samples can be seen in Figures S1, S2, and S3.

With all phases identified, a Rietveld refinement was carried out. For all samples, the internal standard was Al_2O_3, and its exact weight fraction was included for the calculations. The crystal phase parameters k_1 and k_2, which help adjust peak broadening due to microstraining and B_1, which adjusts peak broadening due to crystallite size effects, were adjusted. The spherical harmonics order, which accounts for texture refinement, was also optimized, starting with simpler isotropic refinement and low harmonics orders. Anisotropic refinement and higher harmonics orders were then iteratively implemented to improve the fit until a satisfactory result was achieved. All pattern refinements showed a good fit with χ^2 values below 3.5 for all tests and good visual agreement. The differences between the experimental and calculated patterns were small in all patterns. As an example, the resulting patterns for biochar II can be seen in Figure 7. The $CaCO_3$ content of the original samples (without considering the Al_2O_3) was calculated from the content obtained from each of the three replicate patterns. $CaCO_3$ contents for the biochar samples are shown in Figure 8, along with the Pb^{2+} removal capacity shown above for comparison purposes.

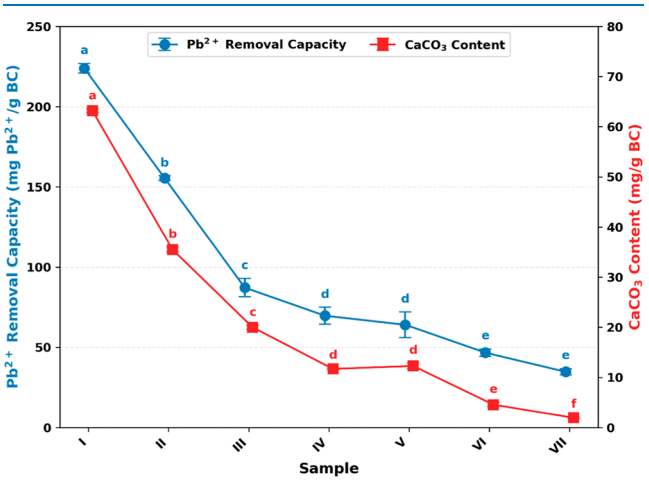

Figure 8. $CaCO_3$ content and Pb^{2+} removal capacity for air curtain burner biochar samples.

It can be seen from these results that all biochar samples are mostly composed of amorphous carbon as expected, but $CaCO_3$ and SiO_2 contents vary greatly between samples, from 63.2 ± 0.4 mg $CaCO_3$ per gram of biochar in biochar sample I to 1.94 ± 0.09 mg $CaCO_3$ per gram of biochar for biochar VII and from over 27.1 ± 0.4 mg SiO_2 per gram of biochar for biochar sample I to 0.3 ± 0.05 mg SiO_2 per gram of biochar for biochar sample III. Compared with the values obtained for Pb^{2+} removal capacity, the trend among the seven samples is the same.

https://doi.org/10.1021/acsomega.6c01646
ACS Omega XXXX, XXX, XXX−XXX

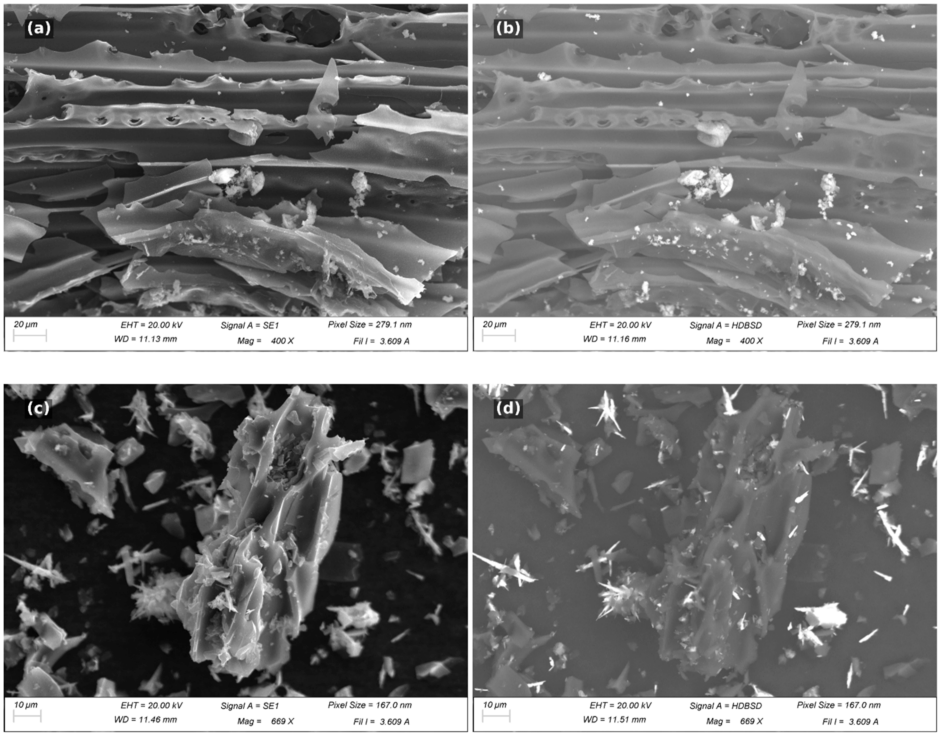

Figure 9. Topographical (SE) and compositional (BSE) analysis of mineral phases. Pristine biochar imaged via (a) SE and (b) BSE detectors. Biochar after Pb^{2+} exposure imaged via (c) SE and (d) BSE detectors.

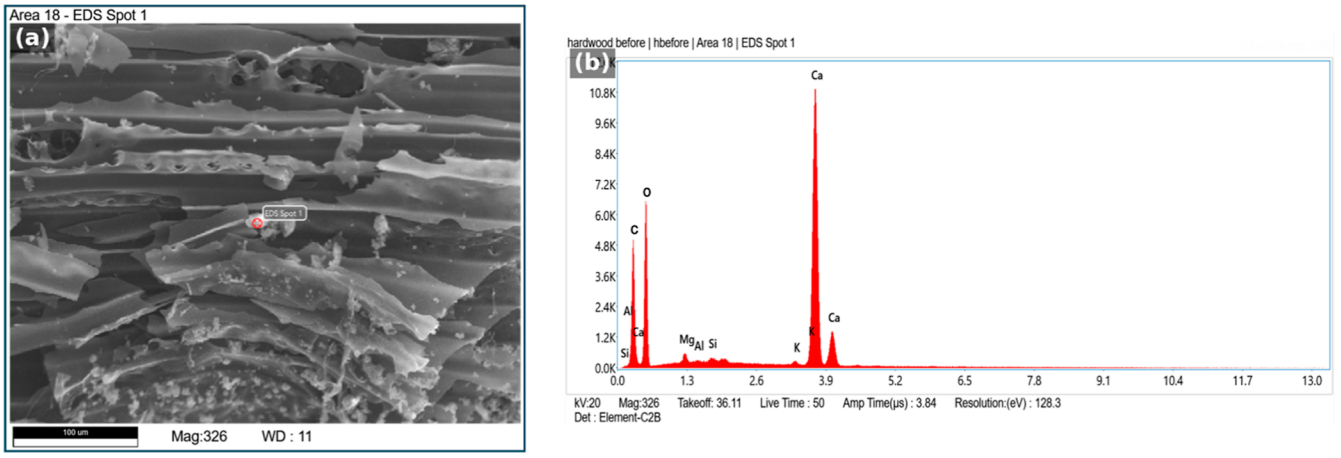

Figure 10. (a) SEM micrograph and (b) corresponding EDS spectrum of the $CaCO_3$ crystal in pristine biochar sample.

3.4. SEM-EDS

3.4.1. Pristine Biochar. Surface morphology and mineral distribution of the pristine biochar were characterized using SE and BSE imaging. Several crystals forming granular aggregates were distributed across the surface of the biochar. SE imaging (Figure 9a) provided topographic detail while BSE imaging (Figure 9b) exhibited high Z-contrast. The high brightness of these crystals relative to the darker carbon matrix indicates the presence of heavier elements. EDS point analysis of these bright regions (Figure 10) confirmed a composition dominated by Ca, C, and O. These results coupled with the XRD scans confirm the presence of $CaCO_3$ crystals in the biochar matrix.

3.4.2. After Pb^{2+} Exposure. SEM analysis revealed that previously observed $CaCO_3$ could not detected. Instead, needle-like crystals were observed both on the carbonaceous matrix as well as by themselves. The needle-like structure matches previous reports of cerussite crystals as seen by SEM.[78] Consistent with the observations of the pristine biochar, SE imaging of the Pb-loaded sample (Figure 9c) revealed crystalline precipitates on the surface while BSE imaging (Figure 9d) showed high contrast between the crystals and the carbon matrix stemming from atomic number differences. EDS point analysis of these new structures (Figure 11) showed a predominant composition of Pb, C, and O.

These results demonstrate that the lead carbonate phases precipitate directly on the biochar surfaces, triggered by the localized dissolution of intrinsic calcite. However, because postexposure Rietveld refinement was not conducted to fully quantify the mass balance of the crystalline phases, the potential occurrence of minor, secondary precipitation within the bulk solution phase cannot be entirely excluded.

https://doi.org/10.1021/acsomega.6c01646
ACS Omega XXXX, XXX, XXX−XXX

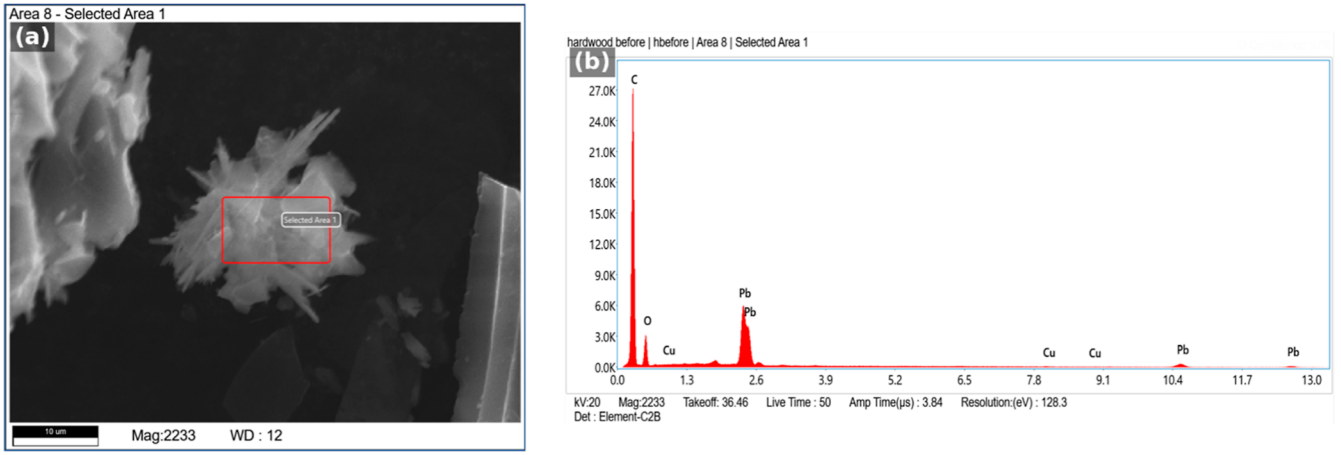

Figure 11. (a) SEM micrograph and (b) corresponding EDS spectrum of the $PbCO_3$ crystal in biochar sample after Pb^{2+} exposure.

3.5. Relationship Between Pb^{2+} Removal Capacity and Biochar Properties

Simple linear regression was performed using the "lm ()" function in R (v4.3.2) to model the relationship between Pb^{2+} removal capacity and measured biochar properties, and to determine which mechanisms are most significant in Pb^{2+} removal. Of the 7 properties investigated, only 2 showed statistical significance ($p < 0.05$): $CaCO_3$ content and O/C ratio. The initial biochar pH was not found to be a statistically significant predictor of removal capacity. This lack of correlation between biochar pH and Pb^{2+} removal capacity suggests that the pH values could have been primarily governed by the solubility equilibrium of $CaCO_3$, with minor pH differences between samples likely arising from secondary ash components or surface functional groups. Because the initial pH characterization was conducted at a high solid-to-liquid ratio, these conditions inherently reflect a highly alkaline environment (pH > 9.9). However, during the actual batch adsorption experiments, the lower biochar-to-solution dosage may result in a less alkaline equilibrium pH. While this native alkalinity establishes a favorable baseline environment for the spontaneous aqueous precipitation of Pb^{2+} into insoluble phases such as $PbCO_3$, the pH itself does not reflect the ultimate removal capacity. Instead, the capacity is governed by the stoichiometric availability of the solid-phase carbonate matrix rather than the equilibrium pH value itself. The pH provides the necessary environment for precipitation but does not reflect the removal capacity, which is governed by the stoichiometric availability of the carbonate rather than the equilibrium pH value itself. EC also showed no correlation with the Pb^{2+} removal capacity, consistent with the trends observed for pH. While an elevated EC indicates the presence of a sufficient ionic environment to initiate lead removal, the instantaneous measurement does not reflect the total $CaCO_3$ available. For ZP, the poor correlation suggests that electrostatic attraction can act as a precursor to removal, but it is not the governing mechanism. In the case of SSA, the lack of correlation indicates that pore-filling and physisorption are not the primary removal mechanisms. While a higher surface area may provide more interface for the initial contact between Pb^{2+} ions and the biochar, the total removal performance was not governed by a physical adsorption process. The regression plots for $CaCO_3$ content and O/C ratio with the best fit line, its confidence interval, and the R^2 coefficient can be seen in Figures 12 and 13.

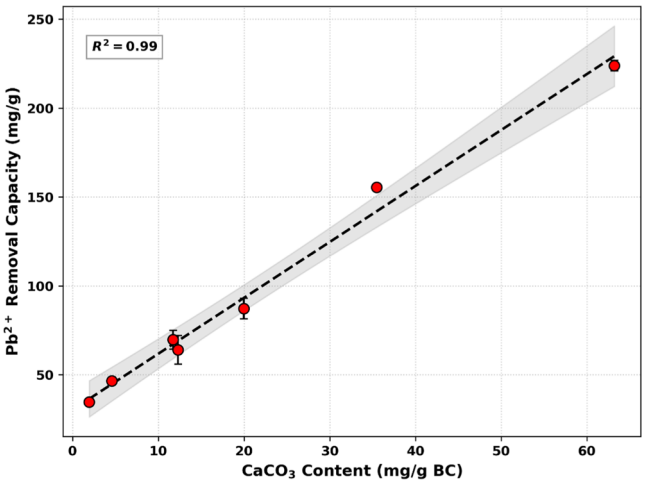

Figure 12. Relationship between the $CaCO_3$ content and the Pb^{2+} removal capacity for all biochar samples, with the confidence interval represented as the shaded area.

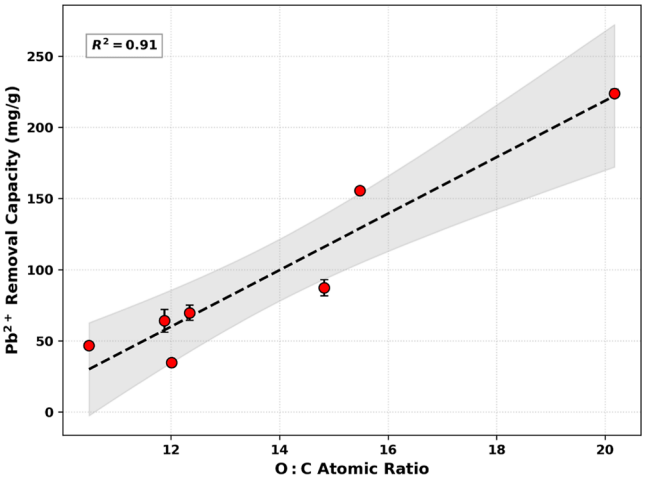

Figure 13. Relationship between O/C ratio and the Pb^{2+} removal capacity for all biochar samples, with the confidence interval represented as the shaded area.

https://doi.org/10.1021/acsomega.6c01646
ACS Omega XXXX, XXX, XXX−XXX

Analysis of the scatter plot and the high R^2 value of 0.99 indicate a very strong and positive relationship between $CaCO_3$ content and Pb^{2+} removal capacity. The positive value of the y-intercept suggests that even if no $CaCO_3$ is present in biochar, Pb^{2+} removal can still occur, probably through other mechanisms such as surface complexation, cation exchange, and electrostatic interactions.[79] This result, alongside the XRD and SEM-EDS results showing the formation of lead carbonate phases, suggests that chemical precipitation could be the primary driver of Pb^{2+} removal in these samples. The O/C ratio also seems to be a good predictor of Pb^{2+} removal capacity. A correlation between O/C ratio and $CaCO_3$ content revealed a strong, positive linear relationship between the biochar's $CaCO_3$ content and its O/C ratio, with a Pearson's correlation coefficient of 0.970 ($p < 0.001$). Given that the presence of $CaCO_3$ is a source of oxygen in the biochar matrix, this relationship is consistent with the hypothesis that the high O/C ratio is primarily a consequence of $CaCO_3$ presence rather than, for example, oxygen-containing surface functional groups. This was confirmed through XRD and SEM-EDS results, indicating the presence of the $CaCO_3$ phases. Additionally, the O content in the biochar sample was calculated by subtracting the masses of C, N, and H from the total mass of the biochar, which also included $CaCO_3$. Therefore, for this study, we focused on $CaCO_3$ content as the primary predictor of Pb^{2+} removal capacity. These results suggest that chemical precipitation is one of the primary, if not the most significant, mechanisms for Pb^{2+} removal by biochar. While the chemical reaction between carbonate and Pb^{2+} has been documented and is recognized as a removal mechanism for lead when using biochar, the present study's quantification of the mineral content in biochar, coupled with its Pb^{2+} removal capacity, sheds new light on the importance of this specific removal pathway.[65,80] While a strong correlation (R^2 = 0.99) was observed between the $CaCO_3$ content and Pb^{2+} removal capacity and the XRD results align with the proposed theory, the statistical limitations inherent in a data set of seven samples are recognized. Biochars produced at different conditions or from different feedstocks may have other mechanisms playing a more significant role. Future studies with a broader selection of samples are necessary to determine if $CaCO_3$ content remains the primary predictor of Pb^{2+} removal across diverse production platforms.

4. CONCLUSIONS

The present work analyzed seven air-curtain burner-produced biochars before and after exposure to Pb^{2+} in solutions, identifying a clear association between the $CaCO_3$ present in the biochar samples and the lead carbonate minerals formed. Additionally, the biochars were characterized by determining their Pb^{2+} removal capacity, zeta potential, pH, electrical conductivity, elemental composition, and $CaCO_3$ content, which was quantified by XRD and Rietveld refinement, a method not previously used to quantify minerals in biochar. This research found strong linear correlations between $CaCO_3$ content and Pb^{2+} removal capacity, suggesting that chemical precipitation is a major contributor to Pb^{2+} removal by these biochars. These findings highlight the significant contribution of intrinsic carbonate phases to biochar's lead remediation capabilities, offering guidance for the design of highly effective biochar remediation agents for environmental applications.

■ ASSOCIATED CONTENT

Data Availability Statement

All relevant data supporting the findings of this study, including the primary experimental results and quantified mineral phase values, are fully contained within the manuscript and its accompanying Supporting Information files. The raw diffraction profile data sets generated during the current study are available from the corresponding author upon reasonable request.

Supporting Information

The Supporting Information is available free of charge at https://pubs.acs.org/doi/10.1021/acsomega.6c01646.

Complete XRD patterns for all pristine samples, after the addition of Al_2O_3 and after $PbCl_2$ exposure (PDF)

■ AUTHOR INFORMATION

Corresponding Author

Yucheng Peng − *College of Forestry Wildlife and Environment, Auburn University, Auburn, Alabama 36849, United States*; Email: yzp0027@auburn.edu

Authors

Juan Tarlera − *College of Forestry Wildlife and Environment, Auburn University, Auburn, Alabama 36849, United States*; orcid.org/0009-0001-6748-4754

Ruiqi Li − *College of Forestry Wildlife and Environment, Auburn University, Auburn, Alabama 36849, United States*

Jonathan Lacuesta − *College of Forestry Wildlife and Environment, Auburn University, Auburn, Alabama 36849, United States*

Haiqiu Jiang − *College of Forestry Wildlife and Environment, Auburn University, Auburn, Alabama 36849, United States*

Tara Keyser − *US Forest Service, Asheville, North Carolina 28801, United States*

Deborah Page-Dumroese − *US Forest Service, Rocky Mountain Research Station, Moscow, Idaho 83843, United States*

Thomas Elder − *College of Forestry Wildlife and Environment, Auburn University, Auburn, Alabama 36849, United States*

Qiangu Yan − *US Forest Service, Forest Products Laboratory, Madison, Wisconsin 53726, United States*

Zhiyong Cai − *US Forest Service, Forest Products Laboratory, Madison, Wisconsin 53726, United States*

Mathew Smidt − *US Forest Service, Southern Research Station, George W. Andrews Forestry Sciences Laboratory, Auburn, Alabama 36849, United States*

Complete contact information is available at: https://pubs.acs.org/10.1021/acsomega.6c01646

Author Contributions

The conceptualization of the study was a joint effort by Juan Tarlera Esteves, Yucheng Peng, and Thomas Elder. Juan Tarlera Esteves was responsible for the methodology, formal analysis, visualization, and wrote the initial draft. Data collection and investigation were conducted by Juan Tarlera Esteves, Ruiqi Li, Jonathan Lacuesta, and Haiqiu Jiang, who also performed data curation. Tara L. Keyser, Deborah Page-Dumroese, Qiangu Yan, Zhiyong Cai, and Mathew Smidt provided the necessary resources for the study. Yucheng Peng and Thomas Elder were responsible for supervision and project

https://doi.org/10.1021/acsomega.6c01646
ACS Omega XXXX, XXX, XXX−XXX

administration, while Yucheng Peng also secured the funding for the research. The manuscript was reviewed and commented on by Juan Tarlera Esteves, Yucheng Peng, and Thomas Elder. The final manuscript was read and approved by all authors.

Funding

This work was supported by the U.S. Forest Service Southern Research Station [grant no. FS-23-JV-11330101−064]; the U.S. Forest Service Southern Research Station [grant no. FS-24-JV-11330101−004], and the College of Forestry, Wildlife and Environment at Auburn University.

Notes

The authors declare no competing financial interest.

REFERENCES

(1) Aziz, K. H. H.; Mustafa, F. S.; Omer, K. M.; Hama, S.; Hamarawf, R. F.; Rahman, K. O. Heavy metal pollution in the aquatic environment: efficient and low-cost removal approaches to eliminate their toxicity: a review. *RSC Adv.* **2023**, *13* (26), 17595−17610.

(2) Saravanan, P.; Saravanan, V.; Rajeshkannan, R.; Arnica, G.; Rajasimman, M.; Baskar, G.; Pugazhendhi, A. Comprehensive review on toxic heavy metals in the aquatic system: sources, identification, treatment strategies, and health risk assessment. *Environ. Res.* **2024**, *258*, 119440.

(3) Fosso-Kankeu, E. Microbial metalloproteins-based responses in the development of biosensors for the monitoring of metal pollutants in the environment. In *Heavy Metals in the Environment: Microorganisms and Bioremediation*; CRC Press, 2018; pp 43−72.

(4) Morais, S.; Costa, F. G.; Pereira, M. d. L. Heavy metals and human health. *Environmental health−emerging issues and practice* **2012**, *10*, 227−245.

(5) Zeitoun, M. M.; Mehana, E. Impact of water pollution with heavy metals on fish health: overview and updates. *Global Vet.* **2014**, *12* (2), 219−231.

(6) Nandakumar, N. P.; Naveenkumar, M.; Senthilkumar, K. Heavy metal harmony: Sustainable solutions for industrial effluent treatment. In *Metal Value Recovery from Industrial Waste Using Advanced Physicochemical Treatment Technologies*; Elsevier, 2025; pp 55−69.

(7) Zafar, S.; Fatima, S.; Asad, F.; Nazir, M. M.; Batool, S.; Ashraf, A. Combating lead (Pb) contamination: integrating biomonitoring, advanced detection, and remediation for environmental and public health. *Water, Air, Soil Pollut.* **2025**, *236* (1), 8.

(8) Bolisetty, S.; Peydayesh, M.; Mezzenga, R. Sustainable technologies for water purification from heavy metals: review and analysis. *Chem. Soc. Rev.* **2019**, *48* (2), 463−487.

(9) Vidu, R.; Matei, E.; Predescu, A. M.; Alhalaili, B.; Pantilimon, C.; Tarcea, C.; Predescu, C. Removal of heavy metals from wastewaters: A challenge from current treatment methods to nanotechnology applications. *Toxics* **2020**, *8* (4), 101.

(10) Ahmed, H. R.; Chawraba, K.; Ealias, A. M.; Kayani, K. F.; Hussain, A. Biocatalytic and enzymatic systems for heavy metal removal from aquatic environments: mechanisms, applications, and future prospects. *Environ. Geochem. Health* **2026**, *48* (3), 128.

(11) Zeng, H.; Jin, B.; Xu, S.; Han, L.; Wang, J.; Jia, H.; Dapaah, M. F.; Cheng, L. Removal of copper, lead and cadmium from water through enzyme-induced carbonate precipitation by soybean urease. *Environ. Res.* **2025**, *277*, 121610.

(12) Fu, F.; Wang, Q. Removal of heavy metal ions from wastewaters: a review. *J. Environ. Manag.* **2011**, *92* (3), 407−418.

(13) Seo, C.; Lee, J. W.; Jeong, J.-W.; Kim, T.-S.; Lee, Y.; Gang, G.; Lee, S. G. Current technologies for heavy metal removal from food and environmental resources. *Food Sci. Biotechnol.* **2024**, *33* (2), 287−295.

(14) Saleh, T. A.; Mustaqeem, M.; Khaled, M. Water treatment technologies in removing heavy metal ions from wastewater: A review. *Environ. Nanotechnol. Monit. Manag.* **2022**, *17*, 100617.

(15) Kumar, V.; Dwivedi, S.; Oh, S. A critical review on lead removal from industrial wastewater: Recent advances and future outlook. *J. Water Process Eng.* **2022**, *45*, 102518.

(16) Ávila, F. G.; Cabrera-Sumba, J.; Valdez-Pilataxi, S.; Villalta-Chungata, J.; Valdiviezo-Gonzales, L.; Alegria-Arnedo, C. Removal of heavy metals in industrial wastewater using adsorption technology: efficiency and influencing factors. *Clean. Eng. Technol.* **2025**, *24*, 100879.

(17) Mandal, S.; Kunhikrishnan, A.; Bolan, N.; Wijesekara, H.; Naidu, R. Application of biochar produced from biowaste materials for environmental protection and sustainable agriculture production. In *Environmental Materials and Waste*; Elsevier, 2016; pp 73−89.

(18) Mohan, D.; Sarswat, A.; Ok, Y. S.; Pittman Jr, C. U. Organic and inorganic contaminants removal from water with biochar, a renewable, low cost and sustainable adsorbent−a critical review. *Bioresour. Technol.* **2014**, *160*, 191−202.

(19) Yang, X.; Zhang, S.; Ju, M.; Liu, L. Preparation and modification of biochar materials and their application in soil remediation. *Appl. Sci.* **2019**, *9* (7), 1365.

(20) Guo, M.; Song, W.; Tian, J. Biochar-facilitated soil remediation: mechanisms and efficacy variations. *Front. Environ. Sci.* **2020**, *8*, 521512.

(21) Sizmur, T.; Quilliam, R.; Puga, A. P.; Moreno-Jiménez, E.; Beesley, L.; Gomez-Eyles, J. L. Application of biochar for soil remediation. In *Agricultural and environmental applications of biochar: Advances and barriers*, 2016; pp 295−324.

(22) Xiang, W.; Zhang, X.; Chen, J.; Zou, W.; He, F.; Hu, X.; Tsang, D. C.; Ok, Y. S.; Gao, B. Biochar technology in wastewater treatment: A critical review. *Chemosphere* **2020**, *252*, 126539.

(23) Gwenzi, W.; Chaukura, N.; Noubactep, C.; Mukome, F. N. Biochar-based water treatment systems as a potential low-cost and sustainable technology for clean water provision. *J. Environ. Manag.* **2017**, *197*, 732−749.

(24) Ennis, C. J.; Evans, A. G.; Islam, M.; Ralebitso-Senior, T. K.; Senior, E. Biochar: carbon sequestration, land remediation, and impacts on soil microbiology. *Crit. Rev. Environ. Sci. Technol.* **2012**, *42* (22), 2311−2364.

(25) Luo, L.; Wang, J.; Lv, J.; Liu, Z.; Sun, T.; Yang, Y.; Zhu, Y.-G. Carbon sequestration strategies in soil using biochar: Advances, challenges, and opportunities. *Environ. Sci. Technol.* **2023**, *57* (31), 11357−11372.

(26) Sahoo, K.; Upadhyay, A.; Runge, T.; Bergman, R.; Puettmann, M.; Bilek, E. Life-cycle assessment and techno-economic analysis of biochar produced from forest residues using portable systems. *Int. J. Life Cycle Assess.* **2021**, *26* (1), 189−213.

(27) Lee, E.; Han, H.-S. Air curtain burners: A tool for disposal of forest residues. *Forests* **2017**, *8* (8), 296.

(28) Puettmann, M.; Sahoo, K.; Wilson, K.; Oneil, E. Life cycle assessment of biochar produced from forest residues using portable systems. *J. Clean. Prod.* **2020**, *250*, 119564.

(29) Page-Dumroese, D. S.; Tirocke, J. M.; Anderson, N. M.; Archuleta, J. G.; McCollum, D. W.; Morisette, J.; Pierson, D. N.; Rodriguez-Franco, C. Continuous in-woods production of biochar using a trailer-mounted air curtain burner. *J. Vis. Exp.* **2024**, *206*, No. e66716.

(30) Li, H.; Dong, X.; da Silva, E. B.; de Oliveira, L. M.; Chen, Y.; Ma, L. Q. Mechanisms of metal sorption by biochars: Biochar characteristics and modifications. *Chemosphere* **2017**, *178*, 466−478.

(31) Ambaye, T. G.; Vaccari, M.; van Hullebusch, E. D.; Amrane, A.; Rtimi, S. Mechanisms and adsorption capacities of biochar for the removal of organic and inorganic pollutants from industrial wastewater. *Int. J. Environ. Sci. Technol.* **2021**, *18* (10), 3273−3294.

(32) Shi, X.; Yang, W.; Li, J.; Yao, Z. The application of biochar as heavy metals adsorbent: the preparation, mechanism, and perspectives. *Int. J. Environ. Res.* **2024**, *18* (3), 41.

(33) Fiorito, E.; Porcedda, G. E.; Brundu, L.; Passiu, C.; Atzei, D.; Ennas, G.; Elsener, B.; Fantauzzi, M.; Rossi, A. Calcium carbonate as sorbent for lead removal from wastewaters. *Chemosphere* **2022**, *296*, 133897.

https://doi.org/10.1021/acsomega.6c01646
ACS Omega XXXX, XXX, XXX−XXX

(34) Shen, T.; Zhong, G.; Wang, L.; Tang, Y. Removal of Pb2+ in aqueous solution by diatom-derived biochar: Role of inherent Ca/Mg minerals. *J. Environ. Chem. Eng.* **2024**, *12* (6), 114760.
(35) Yu, Q.; Liu, H.; Lv, G.; Liu, X.; Wang, L.; Liao, L. Mechanistic insight into lead immobilization on bone-derived carbon/hydroxyapatite composite at low and high initial lead concentration. *Sci. Total Environ.* **2023**, *900*, 165910.
(36) Wnetrzak, R.; Leahy, J.; Chojnacka, K. W.; Saeid, A.; Novotny, E.; Jensen, L. S.; Kwapinski, W. Influence of pig manure biochar mineral content on Cr (III) sorption capacity. *J. Chem. Technol. Biotechnol.* **2014**, *89* (4), 569−578.
(37) Shen, Z.; Hou, D.; Jin, F.; Shi, J.; Fan, X.; Tsang, D. C. W.; Alessi, D. S. Effect of production temperature on lead removal mechanisms by rice straw biochars. *Sci. Total Environ.* **2019**, *655*, 751−758.
(38) Han, R.; Gao, Y.; Jia, Y.; Wang, S. Heterogeneous precipitation behavior and mechanism during the adsorption of cationic heavy metals by biochar: Roles of inorganic components. *J. Hazard. Mater.* **2024**, *480*, 136322.
(39) Yaashikaa, P.; Kumar, P. S.; Varjani, S.; Saravanan, A. A critical review on the biochar production techniques, characterization, stability and applications for circular bioeconomy. *Biotechnol. Rep.* **2020**, *28*, No. e00570.
(40) Bunaciu, A. A.; UdriŞTioiu, E. G.; Aboul-Enein, H. Y. X-ray diffraction: instrumentation and applications. *Crit. Rev. Anal. Chem.* **2015**, *45* (4), 289−299.
(41) Chrysochoou, M.; Dermatas, D. Application of the Rietveld method to assess chromium (VI) speciation in chromite ore processing residue. *J. Hazard. Mater.* **2007**, *141* (2), 370−377.
(42) Liu, H.; Zhao, P.; Wang, S.; Gong, C.; Lu, L. Rietveld quantitative analysis of amorphous phase in slag by internal standard method. In *2018 10th International Conference on Measuring Technology and Mechatronics Automation (ICMTMA)*; IEEEpp 379−382.2018
(43) Bryant, R.; Curi, N.; Roth, C.; Franzmeier, D. Use of an internal standard with differential X-ray diffraction analysis for iron oxides. *Soil Sci. Soc. Am. J.* **1983**, *47* (1), 168−173.
(44) Zhao, P.; Liu, X.; De La Torre, A.; Lu, L.; Sobolev, K. Assessment of the quantitative accuracy of Rietveld/XRD analysis of crystalline and amorphous phases in fly ash. *Anal. Methods* **2017**, *9* (16), 2415−2424.
(45) Šimonová, P. S.ˇ.; Bezdička, P.; Pabst, W. Determination of the content, composition and density of the glass phase in silica refractories and its changes due to thermal cycling. *J. Eur. Ceram. Soc.* **2026**, *46* (9), 118235.
(46) Dai, M. The effect of zeta potential of activated carbon on the adsorption of dyes from aqueous solution: I. The adsorption of cationic dyes: methyl green and methyl violet. *J. Colloid Interface Sci.* **1994**, *164* (1), 223−228.
(47) Peng, Y.; Li, R.; Irfan, M.; Liu, S.; Wang, D.; Elder, T.; Yan, Q.; Cai, Z. Lead ion adsorption by biochar manufactured from downed timber: the effect of downed timber maturity and environmental exposure period. *Wood Mater. Sci. Eng.* **2024**, *1*−*12*.
(48) Ho, Y.-S.; McKay, G. Pseudo-second order model for sorption processes. *Process Biochem.* **1999**, *34* (5), 451−465.
(49) Kılıç, M.; Kırbıyık, C. ¸.; Çepelioğullar, O. ¨.; Pütün, A. E. Adsorption of heavy metal ions from aqueous solutions by bio-char, a by-product of pyrolysis. *Appl. Surf. Sci.* **2013**, *283*, 856−862.
(50) Doebelin, N.; Kleeberg, R. Profex: a graphical user interface for the Rietveld refinement program BGMN. *Appl. Crystallogr.* **2015**, *48* (5), 1573−1580.
(51) Hao, N.; Cao, J.; Ye, J.; Zhang, C.; Li, C.; Bate, B. Content and morphology of lead remediated by activated carbon and biochar: A spectral induced polarization study. *J. Hazard. Mater.* **2021**, *411*, 124605.
(52) Cuevas, J.; Cabrera, M. A.ˇ.; Fernández, C.; Mota-Heredia, C.; Fernández, R.; Torres, E.; Turrero, M. J.; Ruiz, A. I. Bentonite powder XRD quantitative analysis using Rietveld refinement: Revisiting and updating bulk semiquantitative mineralogical compositions. *Miner* **2022**, *12* (6), 772.
(53) Lei, S.; Zhu, L.; Xue, C.; Hong, C.; Wang, J.; Che, L.; Hu, Y.; Qiu, Y. Mechanistic insights and multiple characterizations of cadmium binding to animal-derived biochar. *Environ. Pollut.* **2020**, *258*, 113675.
(54) Chen, W.; Wei, R.; Yang, L.; Yang, Y.; Li, G.; Ni, J. Characteristics of wood-derived biochars produced at different temperatures before and after deashing: their different potential advantages in environmental applications. *Sci. Total Environ.* **2019**, *651*, 2762−2771.
(55) Yargicoglu, E. N.; Sadasivam, B. Y.; Reddy, K. R.; Spokas, K. Physical and chemical characterization of waste wood derived biochars. *Waste Manag* **2015**, *36*, 256−268.
(56) Jiang, S.; Nguyen, T. A.; Rudolph, V.; Yang, H.; Zhang, D.; Ok, Y. S.; Huang, L. Characterization of hard-and softwood biochars pyrolyzed at high temperature. *Environ. Geochem. Health* **2017**, *39* (2), 403−415.
(57) Tomczyk, A.; Sokołowska, Z.; Boguta, P. Biochar physicochemical properties: pyrolysis temperature and feedstock kind effects. *Rev. Environ. Sci. Biotechnol.* **2020**, *19* (1), 191−215.
(58) Singh, B.; Dolk, M. M.; Shen, Q.; Camps-Arbestain, M. Biochar pH, electrical conductivity and liming potential. *Biochar: A guide to analytical methods* **2017**, *23*.
(59) Ani, P. C.; Al-Abedi, H. J.; Smith, J. D.; Zeitoun, Z. Biochar surface chemistry modification by blending hardwood, softwood, and refuse-derived fuel: insights from XPS, FTIR, and zeta potential analysis. *Fuels* **2025**, *6* (3), 71.
(60) Xu, C.-Y.; Li, Q.-R.; Geng, Z.-C.; Hu, F.-N.; Zhao, S.-W. Surface properties and suspension stability of low-temperature pyrolyzed biochar nanoparticles: effects of solution chemistry and feedstock sources. *Chemosphere* **2020**, *259*, 127510.
(61) Fahmi, A. H.; Jol, H.; Singh, D. Physical modification of biochar to expose the inner pores and their functional groups to enhance lead adsorption. *RSC Adv.* **2018**, *8* (67), 38270−38280.
(62) Keiluweit, M.; Nico, P. S.; Johnson, M. G.; Kleber, M. Dynamic molecular structure of plant biomass-derived black carbon (biochar). *Environ. Sci. Technol.* **2010**, *44* (4), 1247−1253.
(63) Pei, L.; Yang, F.; Xu, X.; Nan, H.; Gui, X.; Zhao, L.; Cao, X. Further reuse of phosphorus-laden biochar for lead sorption from aqueous solution: isotherm, kinetics, and mechanism. *Sci. Total Environ.* **2021**, *792*, 148550.
(64) Amin, M.; Alazba, A.; Shafiq, M. Removal of copper and lead using banana biochar in batch adsorption systems: isotherms and kinetic studies. *Arab. J. Sci. Eng.* **2018**, *43* (11), 5711−5722.
(65) Liu, L.; Huang, Y.; Cao, J.; Hu, H.; Dong, L.; Zha, J.; Su, Y.; Ruan, R.; Tao, S. Qualitative and relative distribution of Pb2+ adsorption mechanisms by biochars produced from a fluidized bed pyrolysis system under mild air oxidization conditions. *J. Mol. Liq.* **2021**, *323*, 114600.
(66) Herath, A.; Layne, C. A.; Perez, F.; Hassan, E. B.; Pittman Jr, C. U.; Mlsna, T. E. KOH-activated high surface area Douglas Fir biochar for adsorbing aqueous Cr (VI), Pb (II) and Cd (II). *Chemosphere* **2021**, *269*, 128409.
(67) Wang, H.; Gao, B.; Wang, S.; Fang, J.; Xue, Y.; Yang, K. Removal of Pb (II), Cu (II), and Cd (II) from aqueous solutions by biochar derived from KMnO4 treated hickory wood. *Bioresour. Technol.* **2015**, *197*, 356−362.
(68) Ding, Z.; Wan, Y.; Hu, X.; Wang, S.; Zimmerman, A. R.; Gao, B. Sorption of lead and methylene blue onto hickory biochars from different pyrolysis temperatures: importance of physicochemical properties. *J. Ind. Eng. Chem.* **2016**, *37*, 261−267.
(69) Bardestani, R.; Roy, C.; Kaliaguine, S. The effect of biochar mild air oxidation on the optimization of lead (II) adsorption from wastewater. *J. Environ. Manag.* **2019**, *240*, 404−420.
(70) Mohan, D.; Kumar, H.; Sarswat, A.; Alexandre-Franco, M.; Pittman, C. U. Cadmium and lead remediation using magnetic oak wood and oak bark fast pyrolysis bio-chars. *Chem. Eng. J.* **2014**, *236*, 513−528.

https://doi.org/10.1021/acsomega.6c01646
ACS Omega XXXX, XXX, XXX−XXX

(71) Mohan, D.; Pittman Jr, C. U.; Bricka, M.; Smith, F.; Yancey, B.; Mohammad, J.; Steele, P. H.; Alexandre-Franco, M. F.; Gómez-Serrano, V.; Gong, H. Sorption of arsenic, cadmium, and lead by chars produced from fast pyrolysis of wood and bark during bio-oil production. *J. Colloid Interface Sci.* **2007**, *310* (1), 57−73.
(72) Wang, S.; Gao, B.; Zimmerman, A. R.; Li, Y.; Ma, L.; Harris, W. G.; Migliaccio, K. W. Physicochemical and sorptive properties of biochars derived from woody and herbaceous biomass. *Chemosphere* **2015**, *134*, 257−262.
(73) Boni, M. R.; Chiavola, A.; Marzeddu, S. Remediation of lead-contaminated water by virgin coniferous wood biochar adsorbent: Batch and column application. *Water, Air, Soil Pollut.* **2020**, *231* (4), 171.
(74) Shen, Z.; Zhang, Y.; Jin, F.; McMillan, O.; Al-Tabbaa, A. Qualitative and quantitative characterisation of adsorption mechanisms of lead on four biochars. *Sci. Total Environ.* **2017**, *609*, 1401−1410.
(75) Sahoo, S. S.; Vijay, V. K.; Chandra, R.; Kumar, H. Production and characterization of biochar produced from slow pyrolysis of pigeon pea stalk and bamboo. *Clean. Eng. Technol.* **2021**, *3*, 100101.
(76) Liu, H.; Korshin, G. V.; Ferguson, J. F. Investigation of the kinetics and mechanisms of the oxidation of cerussite and hydrocerussite by chlorine. *Environ. Sci. Technol.* **2008**, *42* (9), 3241−3247.
(77) Davis, A. D.; Webb, C. J.; Sorensen, J. L.; Dixon, D. J.; Hudson, R. Geochemical thermodynamics of lead removal from water with limestone. *Water, Air, Soil Pollut.* **2018**, *229*, 177−7.
(78) Sánchez-Navas, A.; López-Cruz, O.; Velilla, N.; Vidal, I. Crystal growth of lead carbonates: Influence of the medium and relationship between structure and habit. *J. Cryst. Growth* **2013**, *376*, 1−10.
(79) Kypritidou, Z.; El-Bassi, L.; Jellali, S.; Kinigopoulou, V.; Tziritis, E.; Akrout, H.; Jeguirim, M.; Doulgeris, C. Lead removal from aqueous solutions by olive mill wastes derived biochar: Batch experiments and geochemical modelling. *J. Environ. Manag.* **2022**, *318*, 115562.
(80) Ding, W.; Dong, X.; Ime, I. M.; Gao, B.; Ma, L. Q. Pyrolytic temperatures impact lead sorption mechanisms by bagasse biochars. *Chemosphere* **2014**, *105*, 68−74.

https://doi.org/10.1021/acsomega.6c01646
ACS Omega XXXX, XXX, XXX−XXX